Available online at www.sciencedirect.com
SCIENCE DIRECT®
Journal of Solid State Chemistry 177 (2004) 2440–2448
JOURNAL OF SOLID STATE CHEMISTRY
http://elsevier.com/locate/jssc

Synthesis, morphological–structural characterization and magnetic properties of amorphous iron (III)-oxyhydroxy-phosphate nanoparticles

Lorenza Suber,[a,*] Sabrina Foglia,[a] Dino Fiorani,[a] Hector Romero,[a,1] Amelia Montone,[b] Anna Roig,[c] and Lluìs Casas[c]

[a] *CNR-Istituto di Struttura della Materia, Area della Ricerca di Roma 1, Via Salaria km 29,300, 00016 Monterotondo St., Roma, Italy*
[b] *ENEA-INNUMA, C.R. Casaccia, Via Anguillarese km 13, 00060 Roma, Italy*
[c] *Institut de Ciència de Materials de Barcelona (ICMAB-CSIC), Campus de la UAB, Bellaterra, Spain*

Received 29 October 2003; received in revised form 25 March 2004; accepted 29 March 2004

Abstract

The synthesis, the chemical, morphological, structural characterization and the magnetic properties of amorphous iron oxyhydroxy phosphate nanoparticles are reported. Aggregated spherical particles (diameter: 5–12 nm) are obtained showing a ferrihydrite-like behavior similar to that of the bacterial ferritin iron oxyhydroxy-phosphate core. A superparamagnetic behavior is observed with blocking temperatures ranging from ~20 to ~50 K depending on the iron and phosphate content.

Keywords: Ferrihydrite; Ferritin; Iron (III)-oxyhydroxy-phosphate; Iron oxide nanoparticles

1. Introduction

Amorphous metal oxides have relevant industrial applications in a variety of sectors, e.g. in solar energy transformation, magnetic storage media, electronics and catalysis [1]. Furthermore, iron oxide polymers accomplish important functions in biology, agriculture and the environment. In fact, in the first case, iron (III) oxyhydroxy polymers or clusters containing thousands of iron atoms are present as polynuclear aggregates of nanometer dimensions in the protein ferritin and in the related material, hemosiderin. For ferritin isolated from bacterial sources however, a high phosphate content induces the formation of amorphous iron (III) oxyhydroxy phosphate [2].

In agriculture, in iron oxide-rich soils, interaction of phosphate with iron oxide soil minerals leads to a restricted bio-availability of phosphate for plant nutrition [3]. Finally, changes in iron supply to oceanic plankton are thought to have a significant effect on concentrations of atmospheric carbon dioxide, by altering rates of carbon sequestration, the basis of a theory known as the "iron hypothesis" [4].

Despite of many investigations [5–7] reported so far, some aspects, e.g. regarding the composition of the active iron oxide species and the interactions with phosphate ions, need further study. In fact, many research groups in the last 30 years [8] investigated both the mechanism and the formation of iron oxides by hydrolysis and polymerization of iron salts in water. A fascinating result was the comprehension of the role played by counter ions in determining well-defined particle shapes. For example by hydrolysis and polymerization of 3.8×10^{-3} M $FeCl_3$ in aqueous solution at 100°C, rhombohedral hematite crystals (minor and major axis: 18–33 nm) are obtained. The particle shape is determined by the presence of chlorine ions that, as weak complexing agents, induce the particle growth in preferential directions [9]. Other ions can induce morphological transformations. As a matter of fact, an addition in the reaction of small amounts of phosphate

*Corresponding author. Fax: +39-06-90672316.
E-mail address: lorenza.suber@ism.cnr.it (L. Suber).
[1] Permanent address: Dpto de Fisica, Fac de Ciencias, Universidad de Los Andes, Merida Venezuela.

0022-4596/$ - see front matter © 2004 Elsevier Inc. All rights reserved.
doi:10.1016/j.jssc.2004.03.042

ions induce, due to their light adsorption on iron oxide via complexation of Fe^{III}, the formation of *acicular* hematite nanoparticles [10,11] as the final product.

To explore and study the behavior of phosphate ions during the formation of iron oxides, the concentration of phosphate has been varied keeping constant the concentration of the iron salt. Besides crystalline iron oxide and iron oxyhydroxy phases, we have observed the formation of amorphous iron oxyhydroxy phosphate and ferrihydrite nanoparticles. Due to their importance in nature and the scarcity of chemical information in the literature, we have investigated in this work their formation and their morphological–structural and magnetic properties.

2. Experimental

2.1. Material and method

Sodium phosphate monobasic dihydrate p.a. ($NaH_2PO_4 \cdot 2H_2O$) and ferric chloride hexahydrate p.a. ($FeCl_3 \cdot 6H_2O$) were purchased from Acros and Fluka respectively and used as received. The solutions were prepared using Water Plus from Carlo Erba.

Iron oxyhydroxy phoshate particles were prepared by adding to a 1500 mL aqueous solution of 1×10^{-4} M (S1), 2×10^{-4} M(S2), 4×10^{-4} M (S3) and 6.8×10^{-4} M (S4) NaH_2PO_4 at 100°C, 278 mg (6.8×10^{-4} M) $FeCl_3 \cdot 6H_2O$. The reactions were stirred under reflux for 3 days. The precipitates were repeatedly centrifuged and washed with water to remove all extraneous ions. The product yield, referred to iron, was 80–85% (Table 1).

TEM measurements were performed with a JEOL 4000 FX microscope equipped with an Energy Dispersive microscopy (EDS) spectrometer operating at 400 kV.

X-ray diffraction measurements were performed with a SEIFERT XRD 3000 automated powder diffractometer.

TG-DTA measurements were performed with a STA 781 REDCROFT STANTON 1500.

The iron content was determined with an inductively coupled plasma atomic emission spectrometer

Table 1
Experimental conditions for preparation of iron-oxide, -oxyhdroxy, -oxyhydroxy phosphate and ferrihydrite nanoparticles with crystalline phases identified by X-ray diffraction and particle size by TEM

Prep No.	Sample	$FeCl_3$ (M/L)	Na H_2PO_4(M/L)	R: Fe/PO_4	T (°C)	React. time (days)	Phase[a]	Shape[b]	Size[b] (nm)
1		5.4×10^{-2}	1.4×10^{-3}	38.6	100	3	β-FeOOH	Rod[c]	
		[d]			500	1	Amorphous[e]		
2		3.0×10^{-2}	3.8×10^{-4}	79.0	100	10	α-Fe_2O_3	Ac.[f]	400/700
3		2.0×10^{-2}	3.8×10^{-4}	52.6	100	3	α-Fe_2O_3	Ac.	400/90
4		2.0×10^{-2}	3.5×10^{-4}	57.1	100	3	α-Fe_2O_3	Ac.	300/150
5		1.0×10^{-2}	2.6×10^{-4}	38.4	100	3	α-Fe_2O_3	Ac.	90/25
6		1.1×10^{-2}	2.7×10^{-4}	38.6	100	10	α-Fe_2O_3	Ac.	100/200
7		1.1×10^{-2}	5.5×10^{-4}	19.1	100	12	γ-FeOOH	Rod.	150/40
8		6.8×10^{-3}	2.1×10^{-4}	32.3	100	12	γ-FeOOH	Rod.	
9		5.0×10^{-3}	1.0×10^{-4}	50.0	60	7	γ-FeOOH	Rod.	
10		3.8×10^{-3}	9.0×10^{-5}	41.8	100	2	γ-FeOOH	Rod.	
11		3.0×10^{-3}			100	4	α-Fe_2O_3	Rom.[g]	18/33
12		3.0×10^{-3}	8.0×10^{-5}	37.5	100	2	Amorphous	Sph.[h]	See text
13		2.6×10^{-3}	6.4×10^{-5}	40.6	60	10	γ-FeOOH	Rod.	
14		2.1×10^{-3}	6.4×10^{-5}	32.2	60, 100	3, 9	γ-FeOOH	Rod.	500/80
15	S1	6.8×10^{-4}	1.0×10^{-4}	6.8	100	3	Amorphous	Sph.	See text
16	S2	6.8×10^{-4}	2.0×10^{-4}	3.5	100	3	Amorphous	Sph.	See text
17		6.8×10^{-4}	2.0×10^{-4}	3.5	100	30	Amorphous	Sph.	See text
		[d]			600	2 h	Amorphous	Sph.	
18	S3	6.8×10^{-4}	4.0×10^{-4}	1.7	100	3	Amorphous	Sph.	See text
19		6.0×10^{-4}	1.1×10^{-5}	53.1	100	45	γ-FeOOH	Rod.	300/70
20		6.8×10^{-4}	2.0×10^{-4}	3.4	85	15	Amorphous	Sph.	See text
21	S4	6.8×10^{-4}	6.8×10^{-4}	1.0	100	3	Amorphous	Sph.	See text
22		6.8×10^{-4}	1.0×10^{-4}	6.8	85	3	Amorphous	Sph.	See text

[a] Phase determined by X-ray diffraction measurements.
[b] Shape and size determined by TEM measurements.
[c] Rod-like shape.
[d] Thermal treatment of the above reported sample.
[e] Amorphous iron oxyhydroxy phosphate.
[f] Ac.: acicular shape, average size of the minor and major axis, respectively.
[g] Rom.: rhombohedral, average size of the minor and major axis, respectively.
[h] Sph.: spherical.

(Perkin–Elmer), the atomic P/Fe ratio by EDS and the H_2O loss by TG-DTA measurements.

S1: Sp: Fe: 45.6%; P/Fe: 0.16; theoretical for [FeO $(H_2O)_2]_3PO_4 + 1.7$ [$Fe_2O_3 \cdot 1.8$ H_2O]: Fe: 47.9%; P/Fe: 0.16. H_2O loss: sp: −19%, theoretical: −22%.
S2: Sp: Fe: 41.8%; P/Fe: 0.31; theor. for [FeO $(H_2O)_2]_3PO_4 + 0.2$ [$Fe_2O_3 \cdot 1.8$ H_2O]: Fe: 41.5%; P/Fe: 0.29. H_2O loss: sp: −24%, theor: −27%.
S3: Sp: Fe: 36.5%; P/Fe: 0.57; theor. for [$FeO_{0.62}$ $(H_2O)_2]_{1.7}PO_4$: Fe: 35.4%; P/Fe:0.59. H_2O loss: sp: −20%, theor: −23%.
S4: Sp: Fe: 34.7%; P/Fe: 1.2; theor for $FePO_4$: Fe: 37.0%; P/Fe:1. H_2O loss: sp: 0%, theor: 0%.

Infra red measurements were performed with a Perkin–Elmer 16F PC instrument.

UV-visible diffuse reflectance spectra were obtained with a CARY 5 spectrophotometer equipped with an integrating sphere coated with MgO.

Magnetization measurements were carried out by a commercial SQUID magnetometer in the temperature range 5–300 K.

Mössbauer spectrometry was carried out by a conventional transmission Mössbauer spectrometer, using a ^{57}Co source in Rh matrix. Calibration was done using a 25 μm thin natural iron foil.

3. Results

3.1. Chemical, structural and morphological characterization

To study the role of the phosphate ions during the hydrolysis of $FeCl_3$, aqueous solutions of 6.8×10^{-4} M $FeCl_3$ were reacted for 3 days at 100°C in the presence of 1×10^{-4} M (S1), 2×10^{-4} M(S2), 4×10^{-4} M (S3) and 6.8×10^{-4} M (S4) NaH_2PO_4, respectively.

Microanalysis of the iron and phosphorus content and thermogravimetric measurements are consistent, for samples S1 and S2, with the formation of iron oxyhydroxy phosphate [FeO $(H2O)_2]_3$ PO_4 and different amounts of ferrihydrite x[Fe_2O_3 1.8 H_2O] (S1: $x = 1.7$, S2: $x = 0.2$) and for sample S3 with iron oxyhydroxy phosphate [$FeO_{0.62}(H_2O)_2]_{1.7}PO_4$, whereas sample S4 is formed by iron phoshate $FePO_4$ (see the experimental part).

Bright field TEM micrographs evidenced in all samples agglomerates of small particles with diameter of 5–12 nm ca. (Fig. 1). Diffuse rings were observed in all diffraction patterns indicating the presence of disordered structured material; bright spots of about 4 nm are observed in TEM dark field micrographs of S1–S2 samples (Fig. 2) S1 showing the highest fraction. They could indicate the presence of a short range crystalline structure constituted by the 2-line ferrihydrite

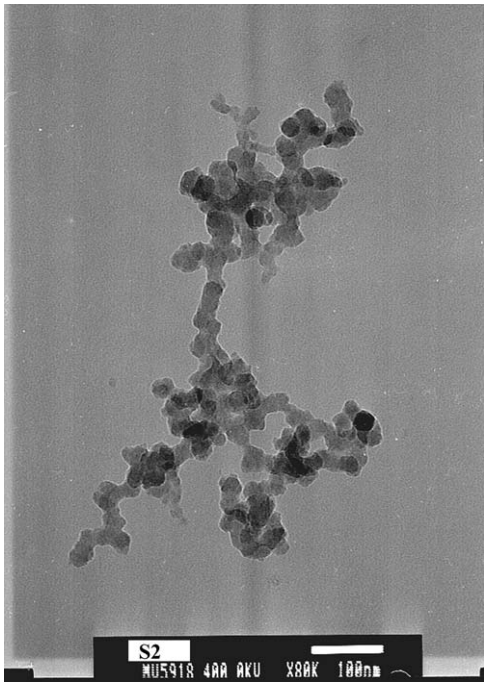

Fig. 1. TEM bright field micrograph of S2.

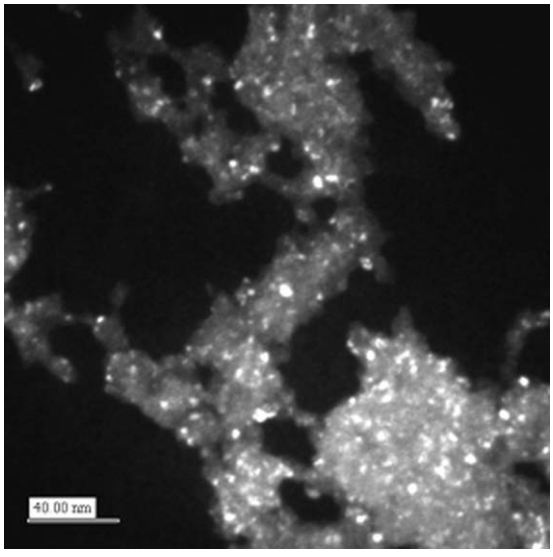

Fig. 2. TEM dark field micrograph of S1.

as supported also by X-ray diffraction measurements (see below).

X-ray diffraction measurements on the as-prepared oxyhydroxy-phosphate particles (S1 and S2) showed only two broad peaks centred at $2\theta = 35$ and $2\theta = 62$ ca., indicating the presence of the 2-line ferrihydrite structure (Fig. 3a), whereas for S3 and S4 no peaks could be identified. When the samples were treated at 1100°C for 5 min, the diffraction measurements revealed, in addition to a broad peak centered at $2\theta = 24$ ca. denoting an amorphous state, peaks attributable to a crystalline Fe_3PO_7 fraction (JCPDS-ICDD 37-61)

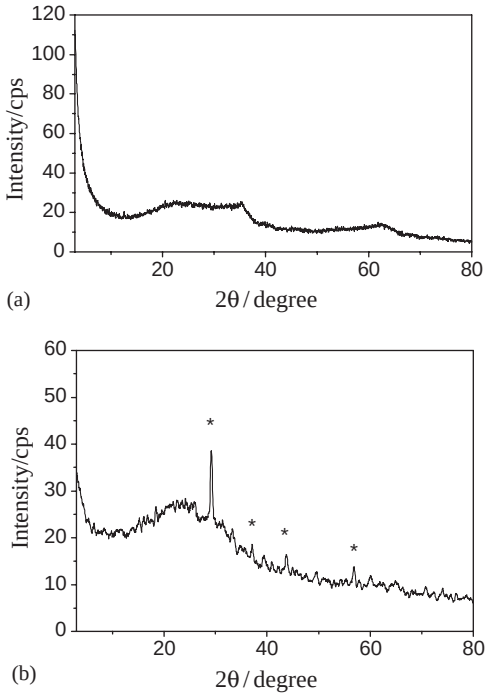

Fig. 3. (a) X-ray diffraction powder spectrum of S2 as prepared and (b) after heating at 1100°C for 5 min.

(Fig. 3b). The formation of iron phosphates after thermal treatment at high temperatures of powders resulting from the reaction of $FeCl_3$ and NaH_2PO_4 is known in the literature [12].

3.2. TG-DTA measurements

The TG and DTA curves of S2 are shown in Fig. 4. The TG curve denotes, in the range 30–200°C, a weight loss of about 19%; no other changes are observed below 1000°C. TG curves of the other samples are similar to that of S2 differing only in the weight loss % (see experimental part). DTA curves of the iron oxyhydroxy phosphate samples S1–S3 are very similar: after two endothermic peaks at 80°C and 130°C, attributable to desorption of water and condensation of hydroxide ligands, respectively, a broad exothermic peak centered at 370°C is present in all samples, probably due to polymerization processes of iron phoshate groups. The two exothermic peaks at 650°C and 720°C can be attributed to solid–solid phase transitions [12].

3.3. IR and UV-visible measurements

In all S1–S4 samples the IR measurements show the presence of broad bands in region 1100–850 cm^{-1} attributable to stretching vibrations of the phosphate groups [13] (Fig. 5). A well-defined strong band at 1262 cm^{-1}, present only in S1, is attributed to P–OH stretching vibration. A strong absorption at 950 cm^{-1}

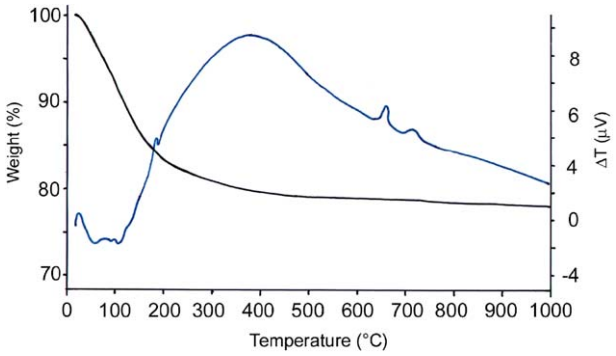

Fig. 4. TG-DTA of S2.

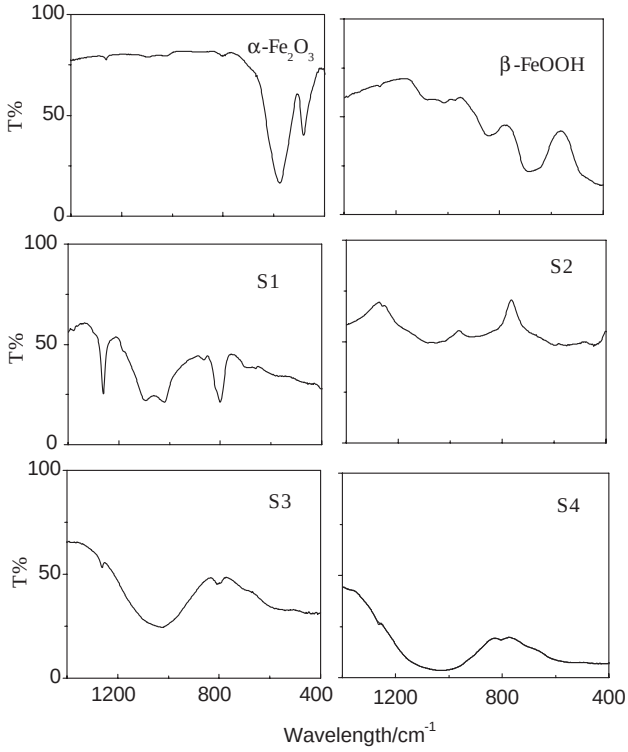

Fig. 5. IR spectra of α-Fe_2O_3, β-FeOOH and S1–S4.

observed in S1 and as a shoulder in the other samples and absent in the α-Fe_2O_3 and FeOOH spectra, is attributed to phosphate vibrations [13]. It is worth noting that when moving from the S1 to S4 samples (i.e. increasing the phosphate content), the bands widen out indicating an increasingly amorphous state. The reflectance (Fig. 6) and the Kubelka Munk remission function spectra (Fig. 7) differ from those of the most common iron oxide and iron oxyhydroxide phases, showing a strong similarity indeed with those of ferrihydrite [14].

3.4. Magnetic susceptibility measurements

The results of magnetization vs. T measurements, performed according the ZFC (zero-field cooling) and FC (field cooling) procedures, are reported in Fig. 8. The curves exhibit the typical features (maximum of

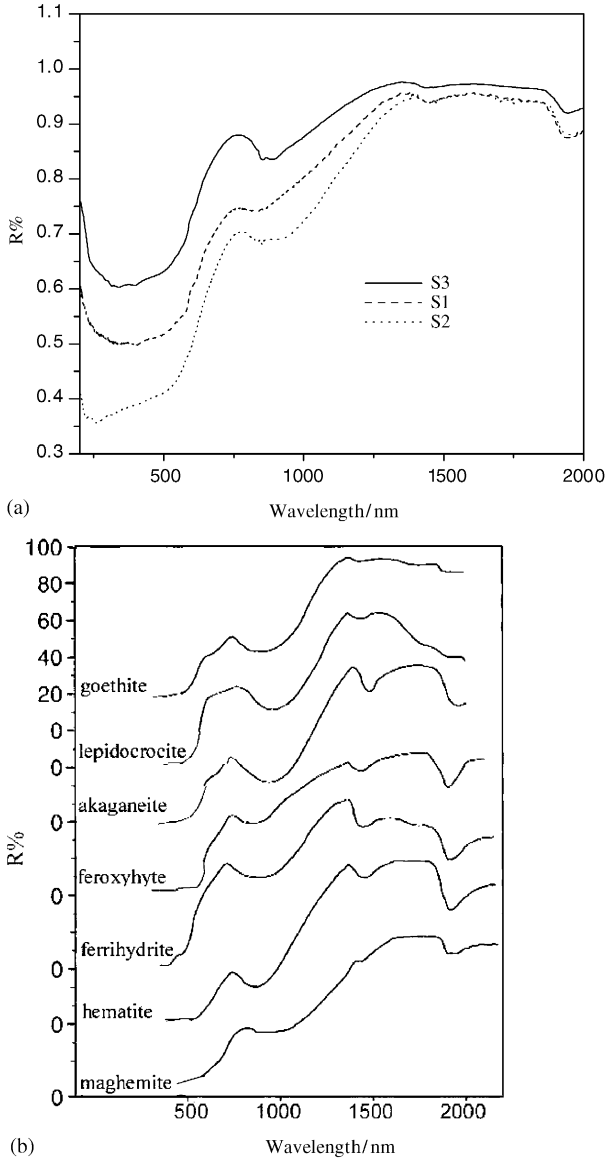

Fig. 6. (a) Reflectance spectra of S1–S3 and (b) reflectance spectra of iron oxides [9].

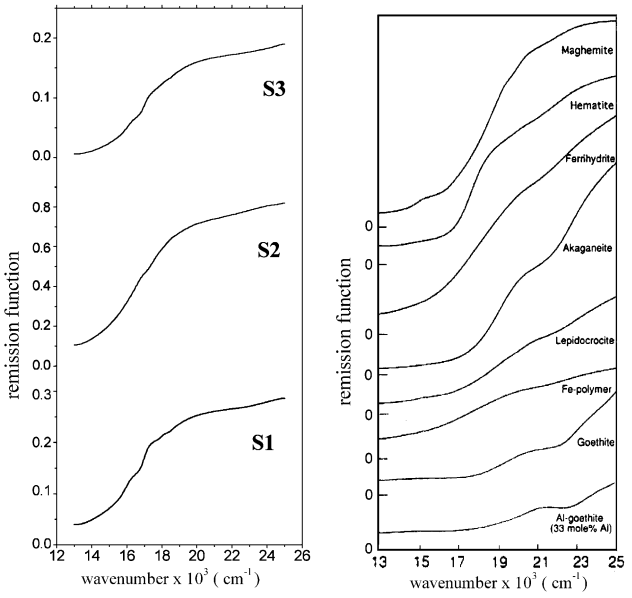

Fig. 7. Kubelka Munk remission function vs. wavelength of S1–S3 and iron oxides [14].

ZFC magnetization, low-temperature splitting between FC and ZFC susceptibility) of an assembly of magnetic nanoparticles whose particle moments thermally fluctuate freely in the high-temperature superparamagnetic state and are blocked at sufficiently low temperatures. For an assembly of independent particles, with volume distribution (V), implying a distribution of anisotropy energy barriers E_B ($E_B = K_a V$ for uniaxial anisotropy) and then of relaxation times (τ) [15], as the temperature decreases, progressively, according to such distribution, the particle moments freeze. The temperature of the ZFC maximum (T_M) is related to the average blocking temperature (T_B) according to relationships which depend on the volume distribution function [16]. For a particle of volume V, with uniaxial anisotropy, $k_B T_B = K_a V \ln t_m/\tau_0$ (k_B is the Boltzmann constant, K_a is the anisotropy constant; t_m is the measuring time; $\tau_0 = 10^{-9}-10^{-11}$ s, according to the Néel–Brown model). Therefore, T_M increases with the average particle volume. In the presence of interparticle interactions, T_M is expected to increase with increasing interaction strength, leading to an increase in the effective anisotropy energy barrier [17].

The results show an increase of T_M with decreasing phosphate content. This reflects an increase of the strength of dipole–dipole interparticle interactions with an increase of the iron/phosphate ratio, i.e. moving from S4 to S1 samples.

The increase of the strength of interparticle interactions is confirmed by the change of the behavior of the FC susceptibility, moving from a Curie like behavior, for sample S4, as expected for independent particles, to a plateau below T_M, as usually observed in strongly interacting particles, showing a collective blocking of moments, as in spin-glasses [18].

The increase of the FC magnetization at low temperature, observed for the S2–S4 samples, suggests the existence of a fraction of still unblocked, very small particles at low temperatures.

Hysteresis cycles at 5 K up to 5 T show no saturation and an increasing coercive field moving from S4 to S1 samples (Fig. 9). This is consistent with the increase of the fraction of the speromagnetic ferrihydrite phase with decreasing phosphate content.

3.5. Mössbauer measurements

The hyperfine parameters deduced from Mössbauer spectra taken at different temperatures are shown in Table 2.

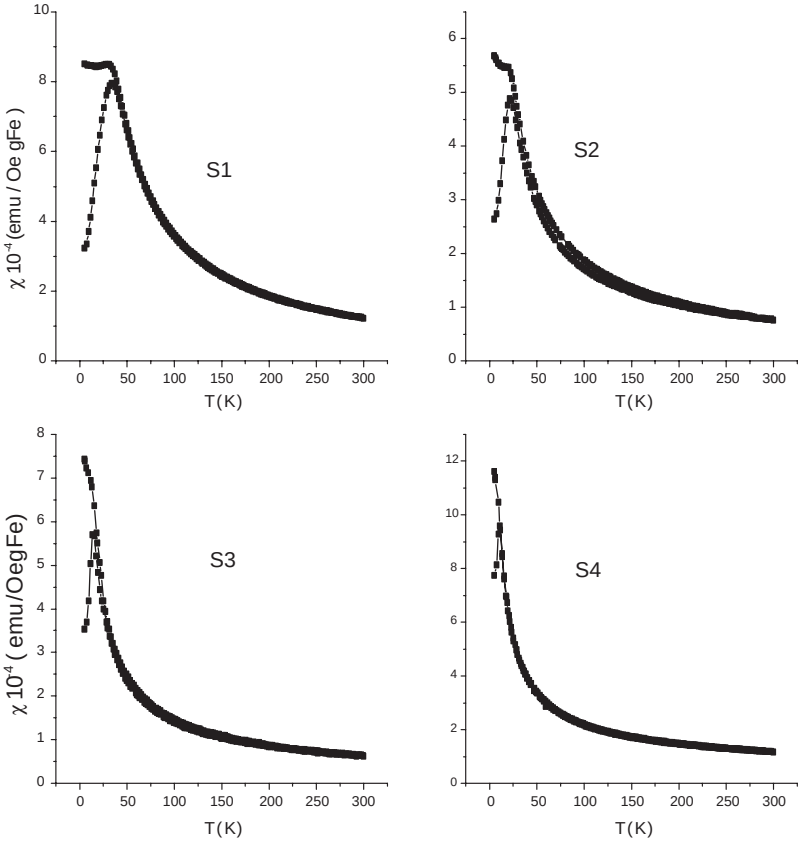

Fig. 8. ZFC-FC susceptibility vs. T ($H = 20$ Oe) of S1–S4.

Spectra taken at 300 and 80 K show a central doublet for all samples. The isomer shift values suggest that iron atoms are in the Fe^{3+} state and although the values are slightly larger than the reported data, they agree quite well with those of ferritin [19] and ferrihydrite [20]. The high value of the quadrupolar splitting (usually 0.5–0.6 in crystalline ferric sites in iron oxides) indicates poor cristallinity and agrees very well with the value of ferryhydrite [19].

The fit values corresponding to the 4.2 K spectra, where all iron atoms are in the blocked state, agree with those of ferryhidrite [15,21]: a negative value for the quadrupolar shift and a low hyperfine field value (clearly ruling out hematite). It must be taken into account that ferritins are a family of iron-storage proteins containing a core of a hydrous ferric oxide-phosphate mineral which is similar in structure to the mineral ferrihydrite. Measurements at 4.2 K confirm the role of phoshate concentration in the formation of iron oxyhydroxy phoshate nanoparticles. The higher the phosphate concentration, the lower the crystallinity fraction of the sample, as it is supported by a decrease in the average hyperfine value and a wider magnetic hyperfine field distribution for sample 3, as seen in Fig. 10.

4. Discussion

A summary of the experimental conditions we have used for the formation of the different iron oxide particles is reported in Table 1. Two main competing factors are responsible for the formation of the different products: (1) the concentration of the $FeCl_3$ salt that determines the magnetic interactions between the primary particles and (2) the ratio $R = [FeCl_3]/[PO_4^{3-}]$ that establish the role of phosphate ions. For high $FeCl_3$ concentrations (10^{-2} M/l) and high R values (80–40), the driving force is the magnetic interaction between iron oxide nuclei, whereas phosphate ions adsorbed on their surface determine the final acicular or rod-like crystalline particle shape [10]. For low $FeCl_3$ concentrations (10^{-4} M/L) and low R values (7–1), the high phosphate concentration leads to the formation of amorphous iron oxyhydroxy phosphate nanoparticles. In the other cases (high $FeCl_3$ concentration and low R values, low $FeCl_3$ concentration and high R values) γ-FeOOH particles are obtained.

For example, it is interesting to compare the preparations 10, 11 and 12 in Table 1: two different iron oxides, lepidocrocite (γ-FeOOH) (prep. 10) and

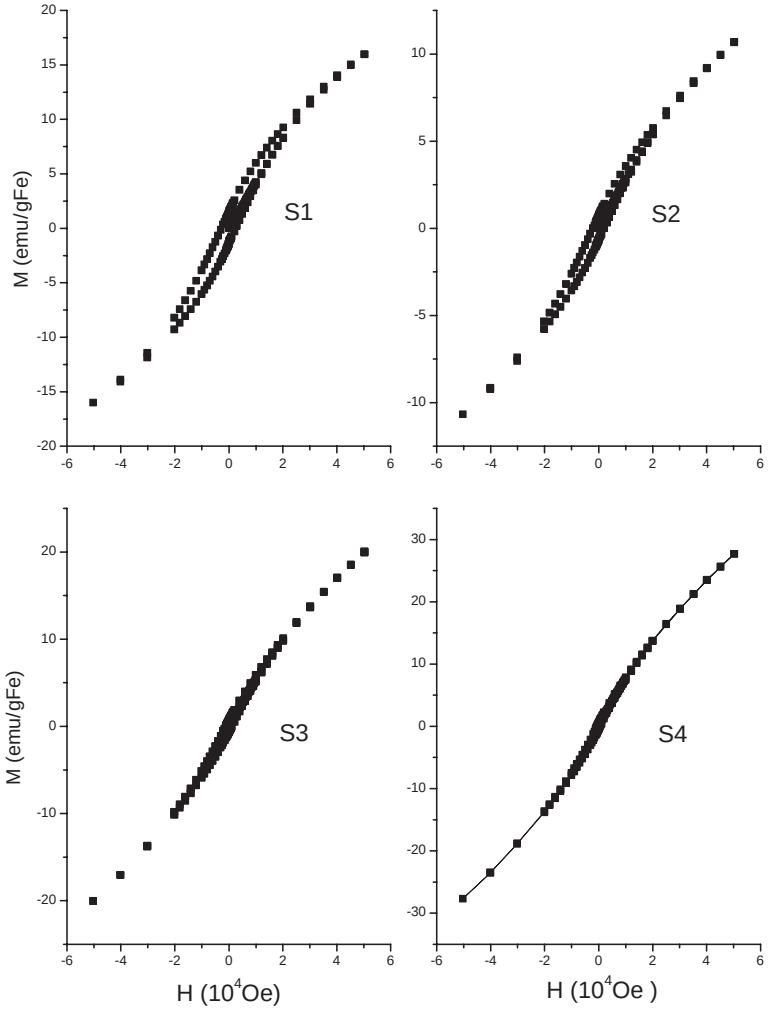

Fig. 9. Magnetization vs. H ($T = 5$ K) of S1–S4.

Table 2
Hyperfine parameters at different temperatures (δ_{Fe} is the isomer shift quoted relative to metallic Fe, Γ is the FWHM value of bands, Δ is the quadrupolar splitting, 2ε the quadrupolar shift of the sextet and $\langle B_{hyp} \rangle$ the mean hyperfine field)

Sample	Temp. (K)	δ_{Fe} (mm/s) (± 0.02)	Γ (mm/s) (± 0.02)	Δ (mm/s) (± 0.02)	2ε (mm/s) (± 0.02)	$\langle B_{hyp} \rangle$ (T) (± 0.05)
S1	300	0.46	0.44	0.69		
	80	0.51	0.56	0.75		
	4.2	0.48			−0.07	48.0
S2	300	0.44	0.52	0.74		
	80	0.56	0.60	0.78		
	4.2	0.47			−0.09	47.7
S3	300	0.47	0.46	0.72		
	80	0.54	0.50	0.76		
	4.2	0.47			−0.08	45.3

amorphous iron oxyhydroxy phosphate nanoparticles (prep. 12) are obtained by comparatively low [PO_4^{-3}] (9×10^{-5} and 8×10^{-5} M, respectively) and [$FeCl_3$] decreasing from 3.8×10^{-3} M to 3×10^{-3} M. A decrease of [Fe^{3+}] determines the prevailing amorphous effect of the phosphate, whereas if phosphate is absent in the reaction (prep. 11), well-defined rhombohedral particles of hematite are obtained.

Finally, it is interesting to note that, among the possible iron oxyhydroxy phases, only γ-FeOOH was

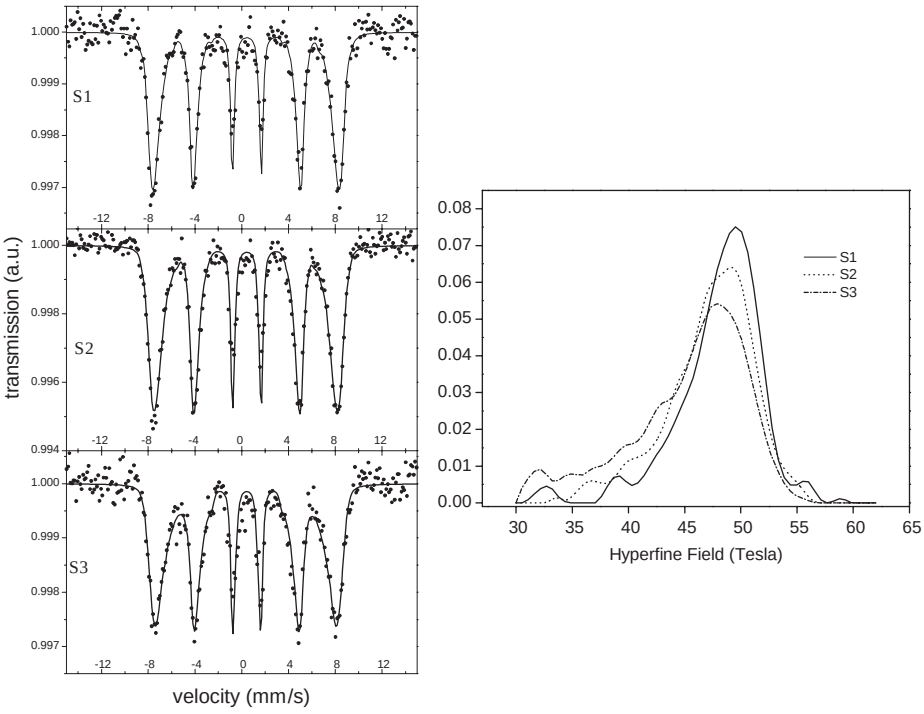

Fig. 10. Mössbauer spectra at 4.2 K of S1–S3.

observed except in prep. 1 (see Table 1) where β-FeOOH agakaneite was formed. In this case, in fact, the Cl^- anions, present in high concentration, fill and stabilize the anion-deficient channels of the β-FeOOH structure [9].

5. Conclusions

By forced hydrolysis of $FeCl_3$ in the presence of NaH_2PO_4, depending upon the reaction conditions, acicular α-Fe_2O_3, γ-FeOOH or amorphous iron (III)-oxyhydroxy-phosphate nanoparticles are obtained. Two main competing factors are responsible for the formation of the different products: (1) the concentration of the $FeCl_3$ salt, that determines the magnetic interactions between the magnetic nanoparticles and (2) the ratio $R=[FeCl_3]/[PO_4^{3-}]$, that determines the role of phosphate ions. In particular, for low $FeCl_3$ concentrations (10^{-4} M/L) and low R values (7–1), the formation of iron oxide is hindered by a phosphate concentration comparable to that of the iron, and amorphous iron oxyhydroxy phosphate is formed. Morphological (TEM), spectroscopic and magnetic (UV-vis, IR, Mössbauer, magnetic susceptibility vs. T and vs H) characterization showed amorphous nanoparticles with a ferrihydrite-like behavior analogous to the bacterial ferritin iron oxyhydroxy-phosphate core. Such particles could represent a good model-material for the study of the bacterial ferritin core.

Acknowledgments

We thank Mr. P. Filaci for magnetization measurements, Mr. C. Veroli for X-ray diffraction measurements, Mr. R. Di Rocco for TG-DTA measurements, Dr. L. Petrilli for microanalysis and Mr. W. Plunkett for revision of the language.

References

[1] M. Ali, Catal. Today 52 (1999) 65–69.
[2] J. Webb, T.G. St Pierre, K.C. Tran, W. Chua-Anusorn, D.J. Macey, P. Pootrakul, Inorg. Chim. Acta 243 (1996) 121–125; S. Mann, J. Bannister, R.J.P. Williams, J. Mol. Biol. 188 (1986) 225–232.
[3] J. Gerke, Geoderma 59 (1993) 279–288.
[4] P.W. Boryd, A.J. Watson, C.S. Law, E.R. Abraham, T. Trull, R. Murdoch, D.C.E. Bakker, et al., Nature 407 (2000) 695–702.
[5] G. Wirnsberger, K. Gatterer, P. Beherens, J. Mater. Chem. 8 (7) (1998) 1509–1510.
[6] M.E. Mata-Zamora, H. Arriola, N. Nava, J.M. Saniger, J. Magn. Magn. Mater. 8 (7) (1996) 161, L6-L10.
[7] W.R. Meyer, S.H. Pulcinelli, C.V. Santilli, A.F. Craievich, J. Non Crys. Solids 273 (2000) 41–47 [and refs. therein].
[8] E. Matijević, P. Sheiner, J. Colloid Interface Sci. 63 (1978) 509; J. Livage, M. Henry, C. Sanchez, Solid State Chem. 18 (1988) 259.
[9] R.M. Cornell, U. Schwertmann, The Iron Oxides, VCH Ed., Weinheim, 1996;
J.K. Bailey, C.J. Brinker, M.L. Mecartney, J. Colloid Interface Sci. 157 (1993) 1–13.
[10] M. Ozaki, S. Krathovil, E. Matijević, J. Colloid, Interface Sci. 102 (1984) 146–151.
[11] L. Suber, D. Fiorani, P. Imperatori, S. Foglia, A. Montone, R. Zysler, Nanostruct. Mater. 11 (1999) 797–803.

[12] A. Modaressi, J. Solid State Chem. 47 (1983) 245;
M.I. Pope, M.D. Judd, Differential Thermal Analysis, Heyden & Son Ltd, London, 1977.
[13] A. Rulmont, R. Cahay, M. Liegeois-Duyckaerts, P. Tarte, Eur. J. Solid State Inorg. Chem. 28 (1991) 207–219;
W. Chua-anusorn, J. Webb, J. Inorg. Biochem. 79 (2000) 303–309.
[14] N. Malengreau, J.P. Muller, G. Calas, Clay and Clay Miner. 42 (1994) 137–147.
[15] J.L. Dormann, D. Fiorani, E. Tronc, Adv. Chem. Phys. 98 (1997) 283.
[16] J.I. Gittleman, B. Abeles, S. Bozowski, Phys. Rev. B 9 (1974) 3891–3897.
[17] J.L. Dormann, L. Bessois, D. Fiorani, J. Phys C 21 (1988) 2015.
[18] D. Fiorani, J.L. Dormann, R. Cherkaoui, E. Tronc, F. Lucari, F. D'Orazio, L. Spinu, M. Nogues, A. Garcia, A.M. Testa, J. Magn. Magn. Mater. 196 (1999) 143–147.
[19] I.P. Suzdalev, A.S. Plachinda, V.N. Buravtsev, Yu.V. Maksimov, S.I. Reiman, V.I. Khromov, D.A. Dmitriev, Chem. Phys. Rep. 17 (1998) 1355.
[20] I.P. Suzdalev, V.N. Buravtsev, V.K. Imshennik, Yu.V. Maksimov, V.V. Matveev, S.N. Novichikhin, A.X. Trautwein, H. Winkler, Z. Phys. 37 (1996) D55.
[21] Q.A. Pankhurst, R.J. Pollard, Clay and Clay Miner. 40 (3) (1992) 268.